nature energy

Supplementary information

https://doi.org/10.1038/s41560-026-02112-8

Iron-mediated reversible lattice-oxygen redox enables stable 200 Wh kg^{-1} sodium-ion batteries

In the format provided by the authors and unedited

Supplementary Figures

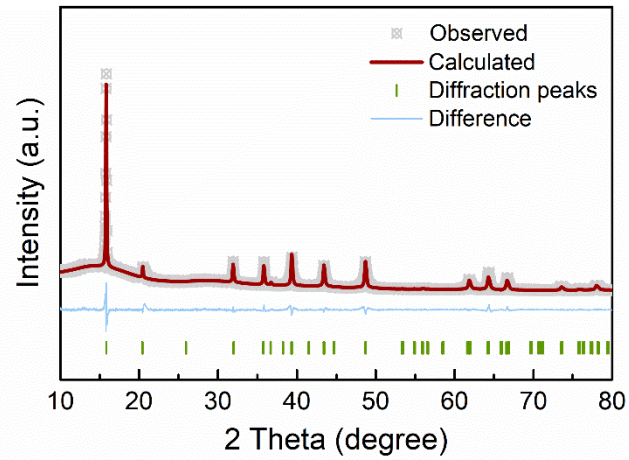

Supplementary Fig. 1 XRD pattern of NMM and corresponding Rietveld refinement plots.

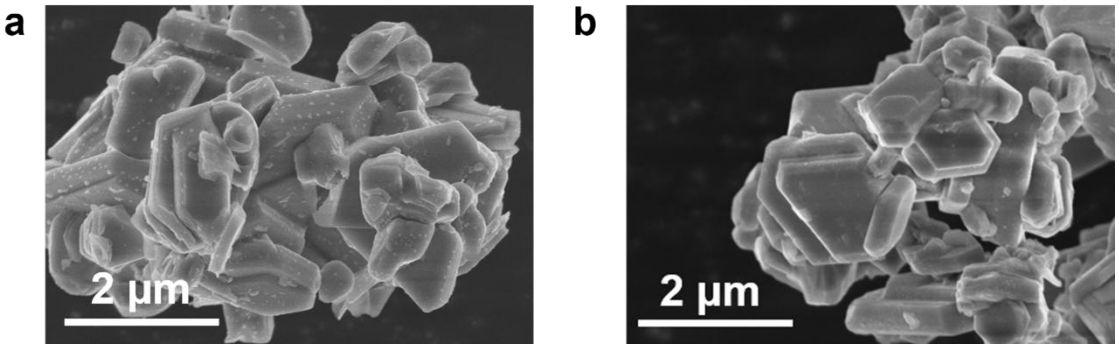

Supplementary Fig. 2 a, **b**, FE-SEM images of NMM (**a**) and NMMF (**b**).

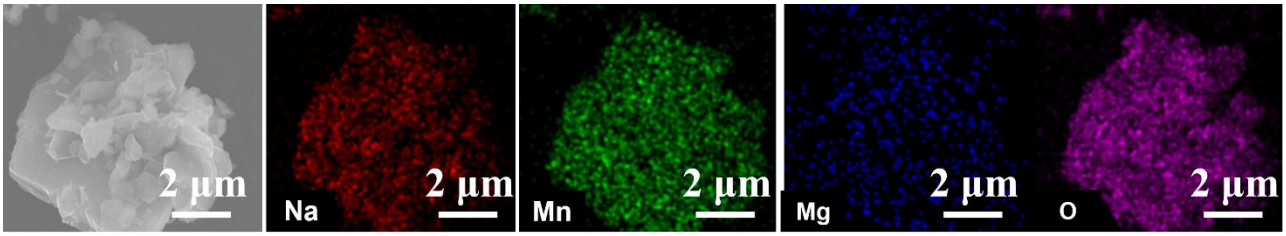

Supplementary Fig. 3 EDS mapping of NMM.

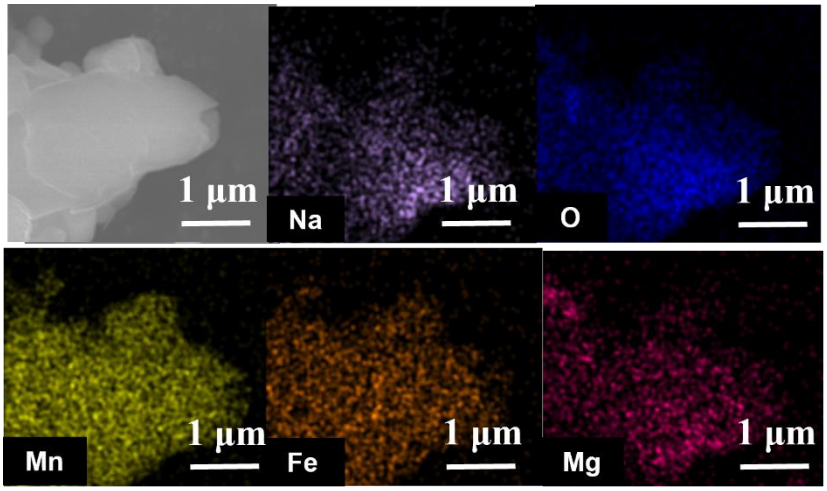

Supplementary Fig. 4 EDS mapping of NMMF.

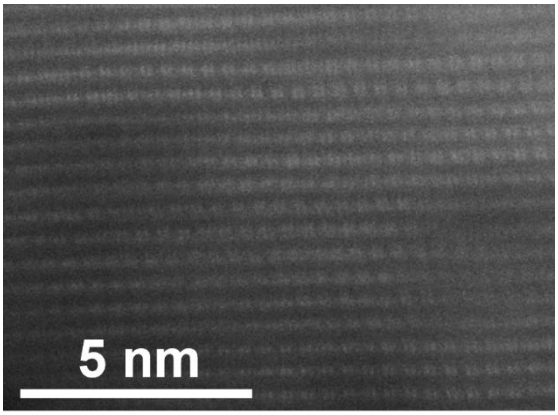

Supplementary Fig. 5 HAADF-STEM image of NMM. A honeycomb superstructure ordering of Li and Mn within the transition metal layer is observed, which aligns with the XRD result.

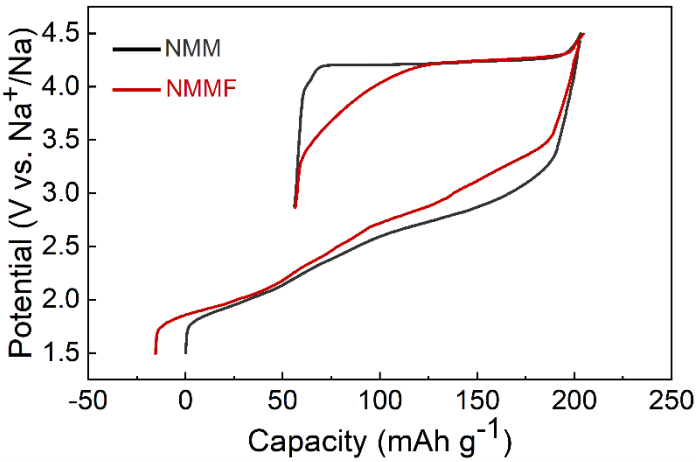

Supplementary Fig. 6 Comparison of the initial charge–discharge curves of NMM and NMMF electrodes.

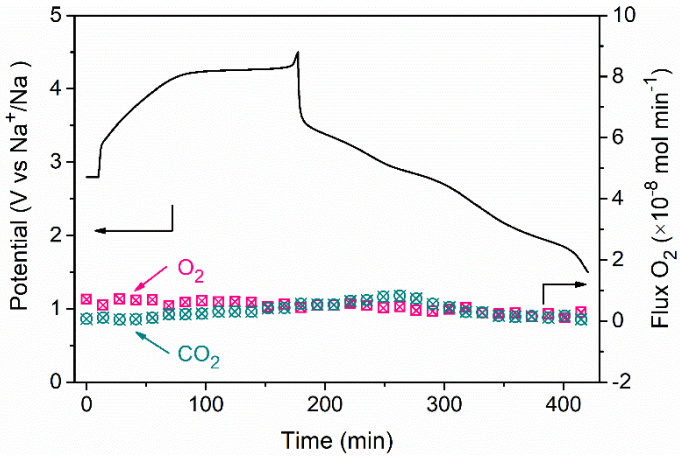

Supplementary Fig. 7 In-situ DEMS result and corresponding charge–discharge curves of NMMF electrode in the first cycle; current density:50 mA g^{-1}; voltage window: 1.5–4.5 V. No oxygen gas was detected in the entire charge–discharge process.

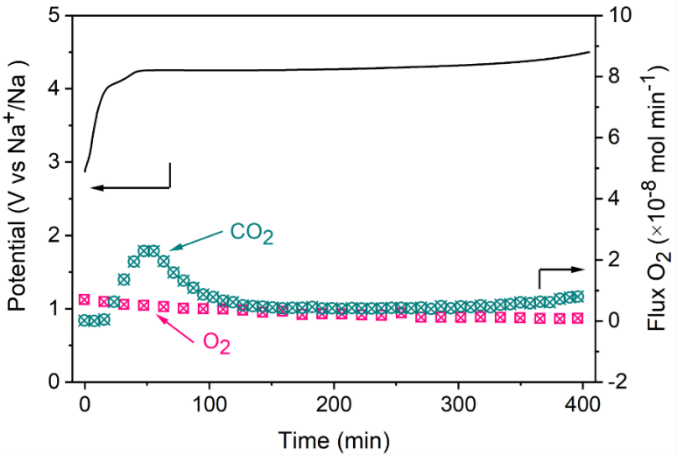

Supplementary Fig. 8 In-situ DEMS result and corresponding charge curve of NMM electrode in the first cycle; current density:20 mA g^{-1}; voltage window: 1.5–4.5 V. No oxygen gas was detected in the entire charge process.

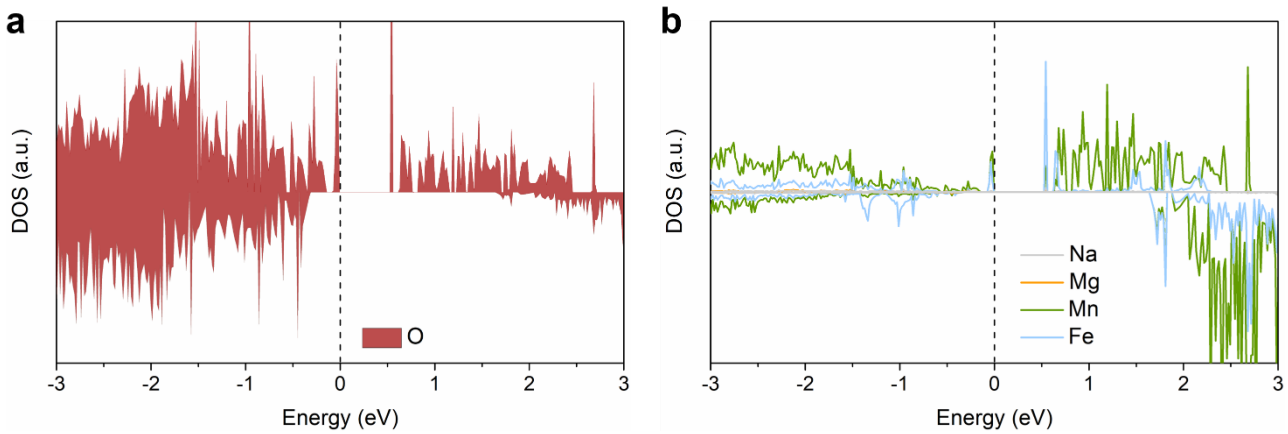

Supplementary Fig. 9 The DOSs of $Na_{16}Mn_{14}Mg_6Fe_4O_{48}$ supercell. **a**, The pDOS of O. **b**, The pDOSs of Mn, Mg, Fe and Na. The green, orange, blue and gray lines represent the pDOSs of Mn, Mg, Fe and Na, respectively.

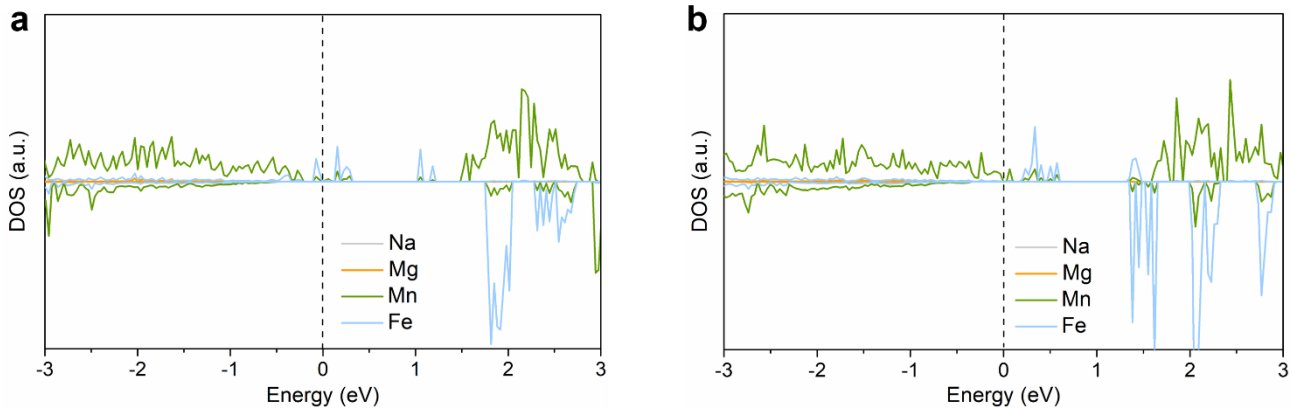

Supplementary Fig. 10 a,**b**, The pDOSs of Mn, Mg, Fe and Na in $Na_8Mn_{14}Mg_6Fe_4O_{48}$ (**a**) and $Na_4Mn_{14}Mg_6Fe_4O_{48}$ (**b**) supercells. The green, orange, blue and gray lines represent the pDOSs of Mn, Mg, Fe and Na, respectively.

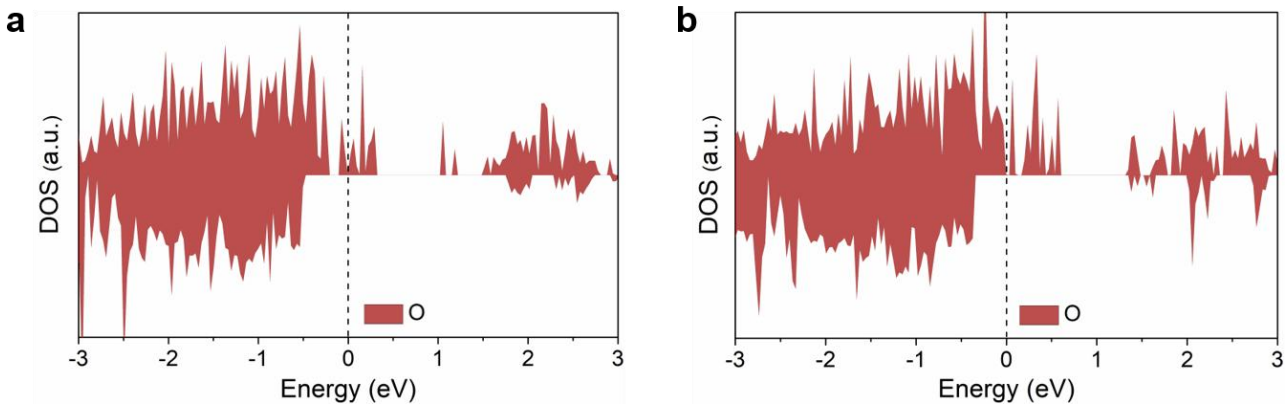

Supplementary Fig. 11 a, **b**, The pDOSs of O in $Na_8Mn_{14}Mg_6Fe_4O_{48}$ (**a**) and $Na_4Mn_{14}Mg_6Fe_4O_{48}$ (**b**) supercells. The similar electronic structures of the O in the two supercells are consistent with the high redox reversibility.

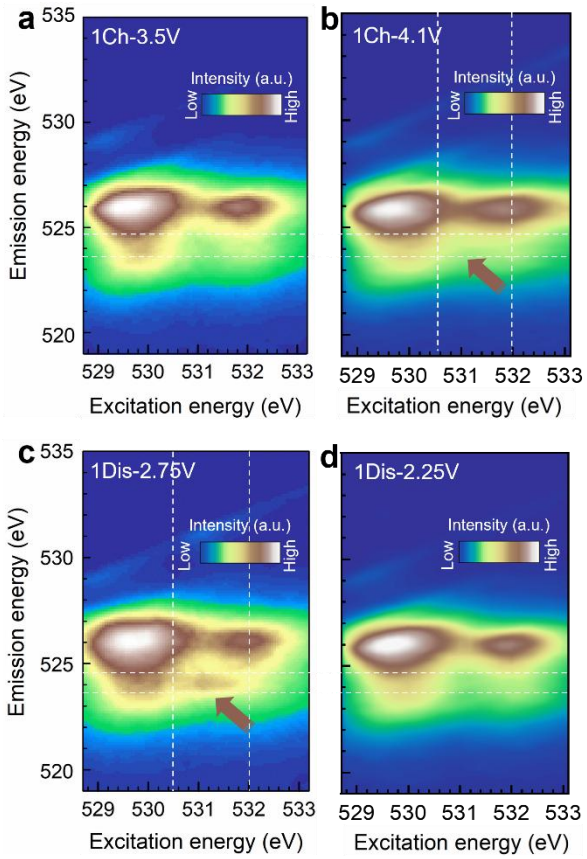

Supplementary Fig. 12 a-d, O-*K* mRIXS of NMMF electrodes at different states during the initial cycle: charged to 3.5 V (**a**) and 4.1 V (**b**), respectively; discharged to 2.75 V (**c**) and 2.25 V (**d**), respectively. The arrows at an emission energy of 523.7 eV and an excitation energy of 531.0 eV indicate the oxidized lattice oxygen features in desodiated state.

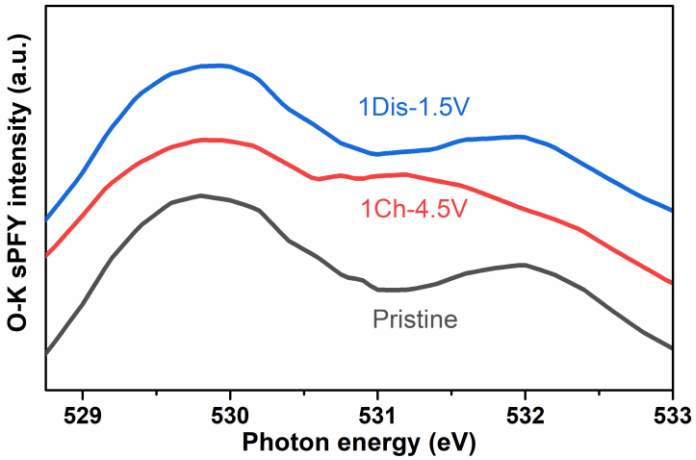

Supplementary Fig. 13 sPFY spectra extracted from O-*K* mRIXS (Fig. 2a-c) by integrating the 523.7 eV emission energy range.

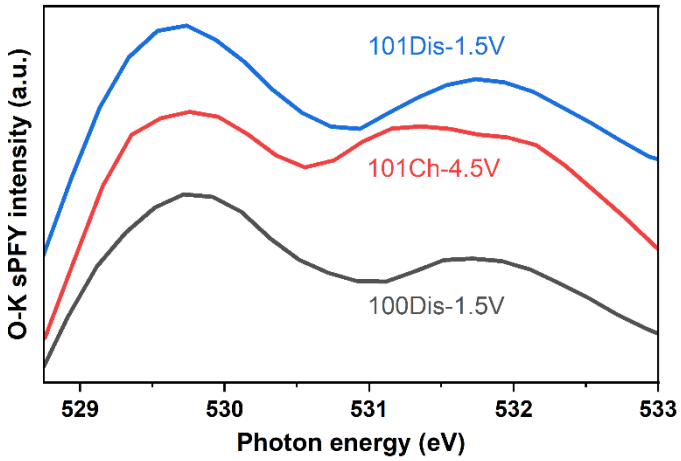

Supplementary Fig. 14 sPFY spectra extracted from O-*K* mRIXS (Fig. 2e-g) by integrating the 523.7 eV emission energy range.

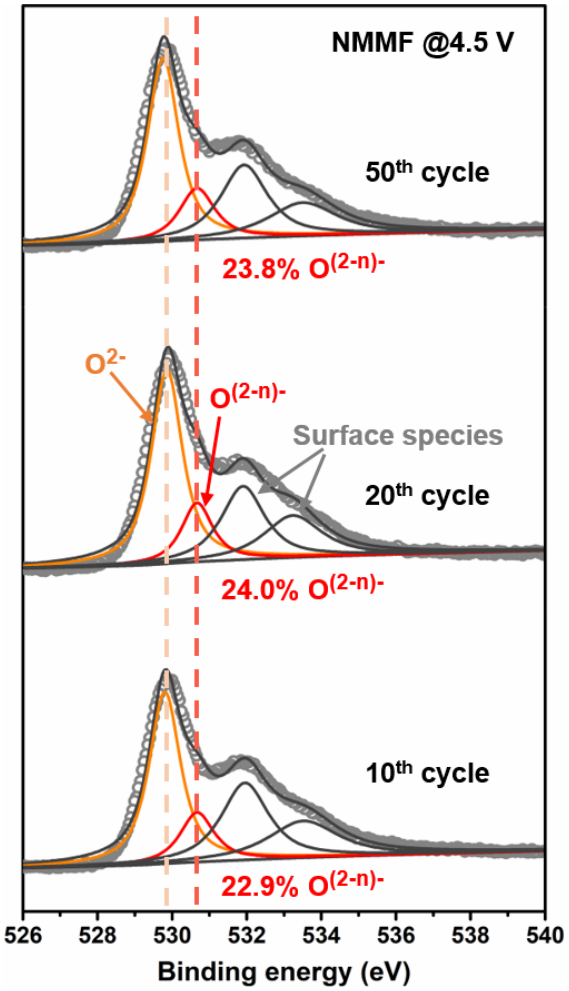

Supplementary Fig. 15 XPS spectra of fully charged NMMF electrodes (Ch-4.5V) in the 10th (down), 20th (middle) and 50th (up) cycles; current density: 50 mA g^{-1}; potential window: 1.5-4.5 V. All the samples had been etched 20 nm before XPS testing. The deconvolution of O 1s can be attributed to lattice oxygen (O^{2-}, orange) at around 529.7 eV, oxidized lattice oxygen ($O^{(2-n)-}$, red) at around 530.6 eV, and surface oxygenated specices (black)[S1,S2].

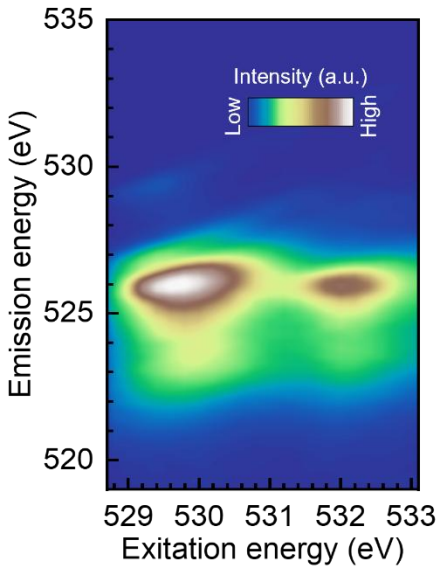

Supplementary Fig. 16 O-*K* mRIXS of NMM electrode charged to 4.1 V.

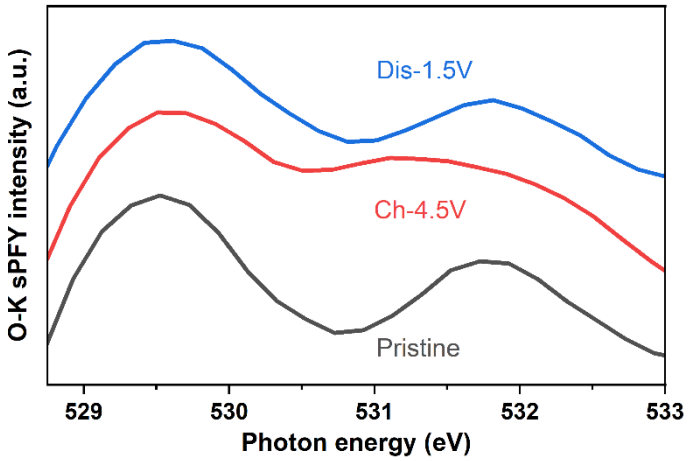

Supplementary Fig. 17 sPFY spectra extracted from O-*K* mRIXS (Fig. 2i-k) by integrating the 523.7 eV emission energy range.

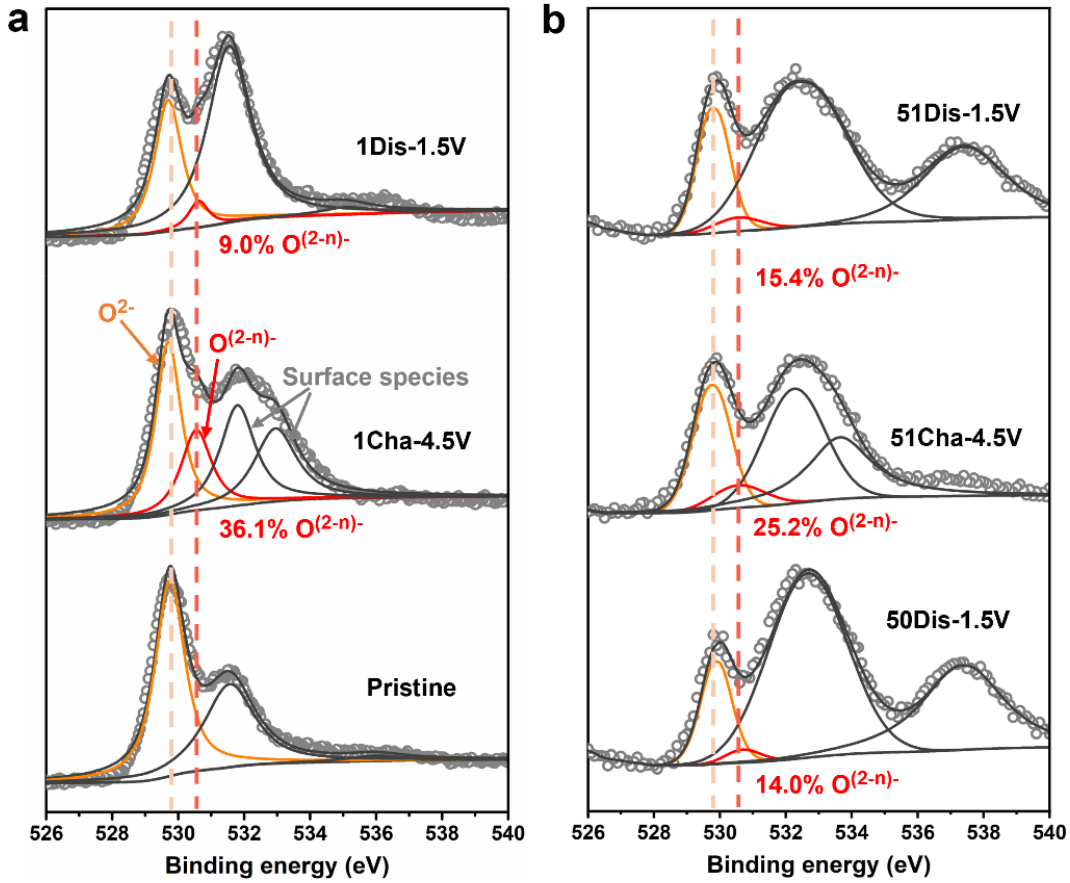

Supplementary Fig. 18 a, XPS spectra of NMM electrodes in the pristine state, the fully charged state (1Cha-4.5V), and fully discharged state (1Dis-1.5V) during the 1st cycle. **b**, XPS spectra of cycled NMM electrodes in the pristine state (50Dis-1.5V), the fully charged state (51Cha-4.5V), and the fully discharged state (51Dis-1.5V) during the 51th cycle. Analysis of these spectra indicates that the reversibility of the lattice oxygen redox reaction in NMM is approximately 75% in the initial cycle, consistent with mRIXS observations. After 50 cycles, the reversibility increases to about 88%. This apparent improvement, however, should be interpreted within the broader electrochemical context: while oxygen redox reversibility improves, its overall activity decreases significantly upon cycling, resulting in a reduced absolute contribution to the reversible capacity. This behavior aligns with the poor long-term cycling stability of NMM, demonstrating that although the oxygen redox reaction becomes more reversible to a limited extent after cycling, its actual participation and contribution to the total capacity are substantially diminished.

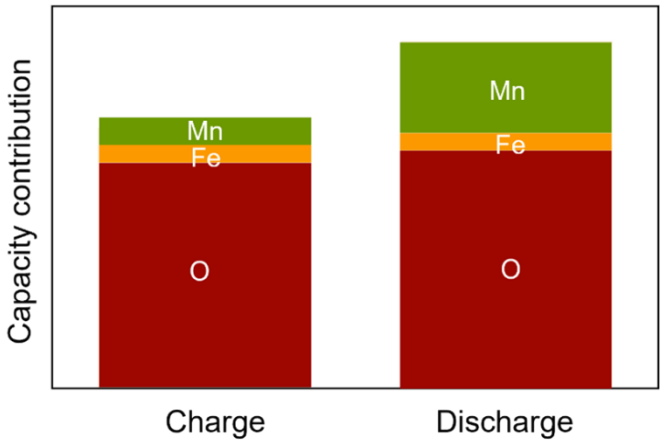

Supplementary Fig. 19 Capacity contributions from Mn, Fe, and O, as quantified based on the evolution of oxidation states from in situ XANES during the first cycle. For the pristine material, the fitted oxidation states were $Mn^{3.8+}$ and $Fe^{3.0+}$. Extending this analysis to the fully charged and fully discharged states gave values of $Mn^{3.9+}$ and $Mn^{3.6+}$ for Mn, and $Fe^{3.2+}$ and $Fe^{3.0+}$ for Fe, respectively.

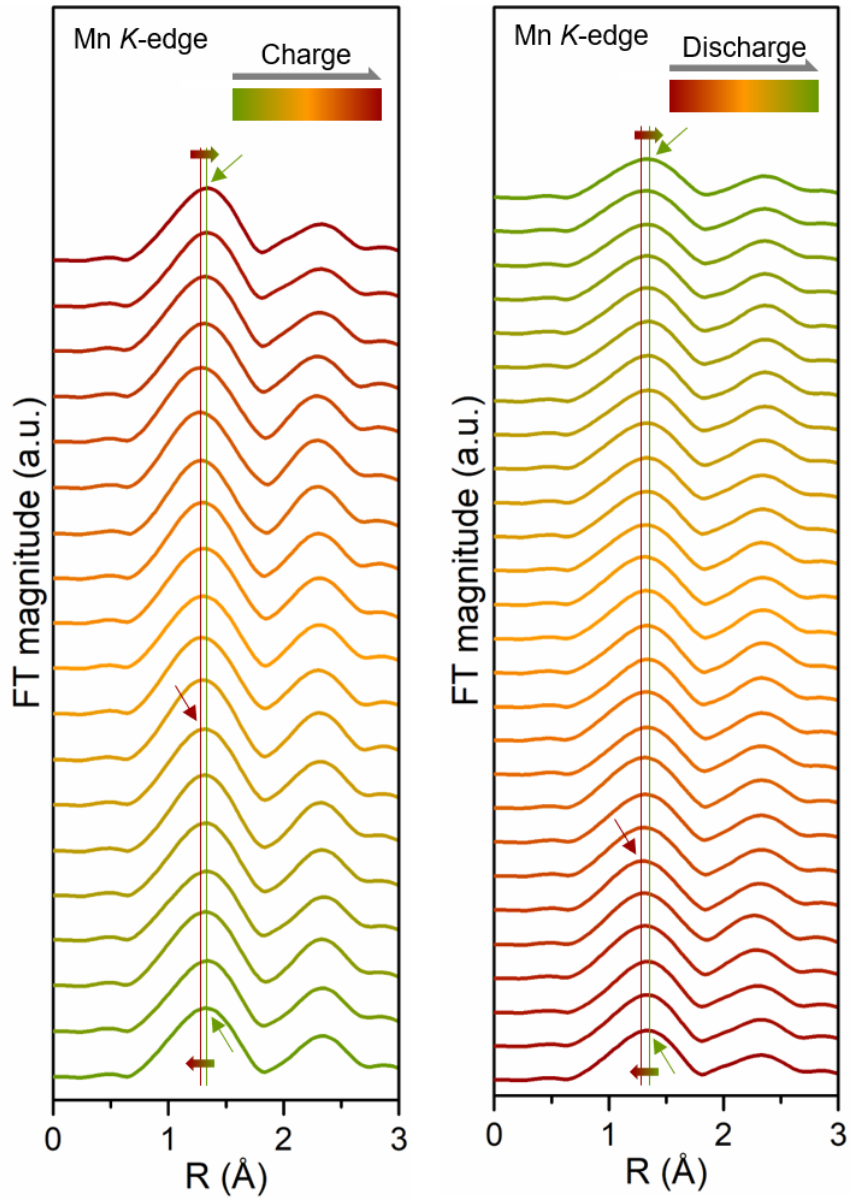

Supplementary Fig. 20 In-situ Mn K-edge Fourier transformed EXAFS spectra of NMMF during the 1st charge (left) and discharge (right) processes. During the charging process, the peak position shifts from 1.36 Å to 1.27 Å and then returns to 1.36 Å for Mn-O bonding. This shift is attributed to the oxidation of Mn at the beginning of charging, causing a contraction of the Mn-O bond. As charging progresses, lattice oxygen participates in the oxidation, leading to elongation of the Mn-O bond. During the discharge process, the peak position shifts from 1.36 Å to 1.26 Å and then returns to 1.36 Å. This can be attributed to the reduction of oxidized lattice oxygen at the beginning of discharging, resulting in a contraction of the Mn-O bond[S3,S4]. As discharging continues, Mn^{4+} is reduced to Mn^{3+}, leading to elongation of the Mn-O bond. Notably, compared to the pristine state, the lattice oxygen in the discharged state is restored to O^{2-}, and Mn is more reduced to Mn^{3+}. However, the Mn-O bond lengths remain almost unchanged, indicating more $Mn^{3+}O_6$ Jahn-Teller distortions in the discharged state[S5,S6].

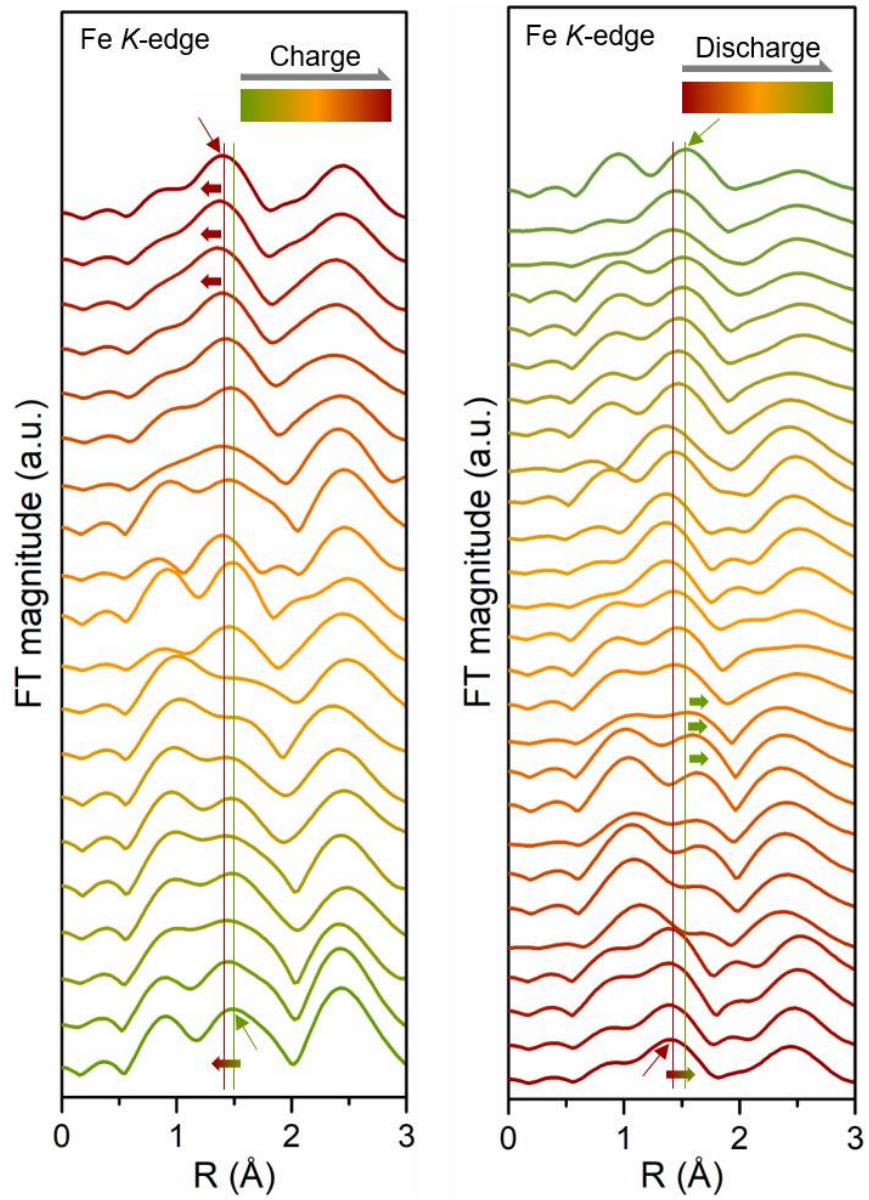

Supplementary Fig. 21 In-situ Fe K-edge Fourier transformed EXAFS spectra of NMMF during the 1st charge (left) and discharge (right) processes. The red horizontal arrows indicate that the Fe-O bond length during the late charging stage (1.35 Å) is smaller than the bond length of the final charged state (1.40 Å). The green horizontal arrows indicate that the Fe-O bond length in the discharged intermediate state (1.67 Å) is larger than that in the final discharged state (1.49 Å). The peak position shifts from 1.49 Å in the origin state to 1.40 Å in the full charge for Fe-O bonding during the charging process. This shift is attributed to the oxidation of Fe^{3+} to Fe^{4+}, leading to a contraction of the Fe-O bond. However, there are irregular shifts in the peak position during the process. Specifically, in some charge states (1.35 Å), the Fe-O bonding is shorter than in the full charge state (1.40 Å). This can be attributed to the oxidation of lattice oxygen[S4] and electronic exchange between Fe^{4+} and O^{2-}[S7,S8]. During the discharge process, the peak position shifts from 1.40 Å in the full charge state to 1.49 Å in the full discharge, attributed to the reduction of Fe^{4+} to Fe^{3+}, resulting in elongation of the Fe-O bond. However, in some discharge states (1.67 Å), the Fe-O bonding is longer than in the full discharge state (1.49 Å), which can be attributed to the reduction of lattice oxygen and electronic exchange between Fe^{2+} and $O^{(2-n)-}$[S1,S9,S10].

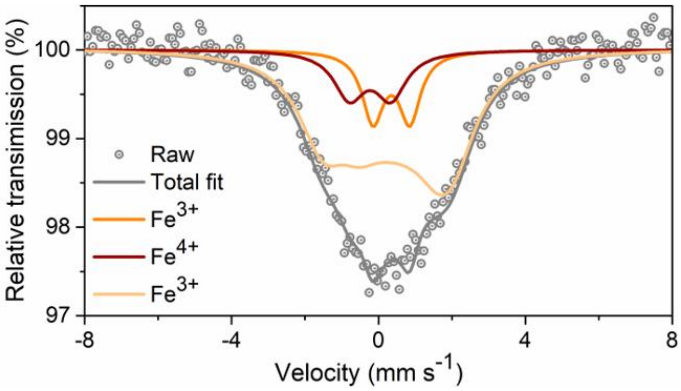

Supplementary Fig. 22 77 K ^{57}Fe Mössbauer spectra of the Ch-4.25V NMMF electrode in the velocity of -8 – 8 mm s^{-1}. The results of the higher-resolution 77 K ^{57}Fe Mössbauer spectra are consistent with those of the room temperature ^{57}Fe Mössbauer spectra results, and all the Fe is located in the FeO_6 octahedral. The detailed sub-spectra of the low temperature ^{57}Fe Mössbauer spectra here are similar to those of the previous $Na_xMn_{0.5}Fe_{0.5}O_2$ reported by Shinichi Komada et al.[S11].

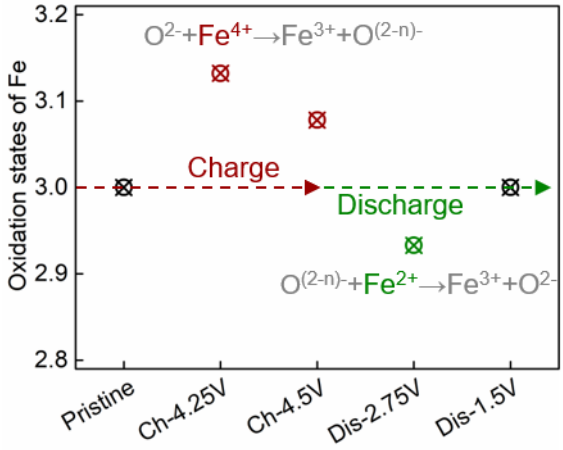

Supplementary Fig. 23 A summary of Fe oxidation states under various charge/discharge states, derived from the ^{57}Fe Mössbauer spectra results presented in Fig. 4a. For the bifunctional iron RM in NMMF, during the charge process, the highly oxidative Fe^{4+} can capture electrons from lattice-oxygen with non-bonding O 2p orbitals ($O^{2-} + Fe^{4+} \rightarrow O^{(2-n)-} + Fe^{3+}$). In the discharge process, the electrons from reductive Fe^{2+} can be captured by the oxidized lattice-oxygen ($O^{(2-n)-} + Fe^{2+} \rightarrow O^{2-} + Fe^{3+}$).

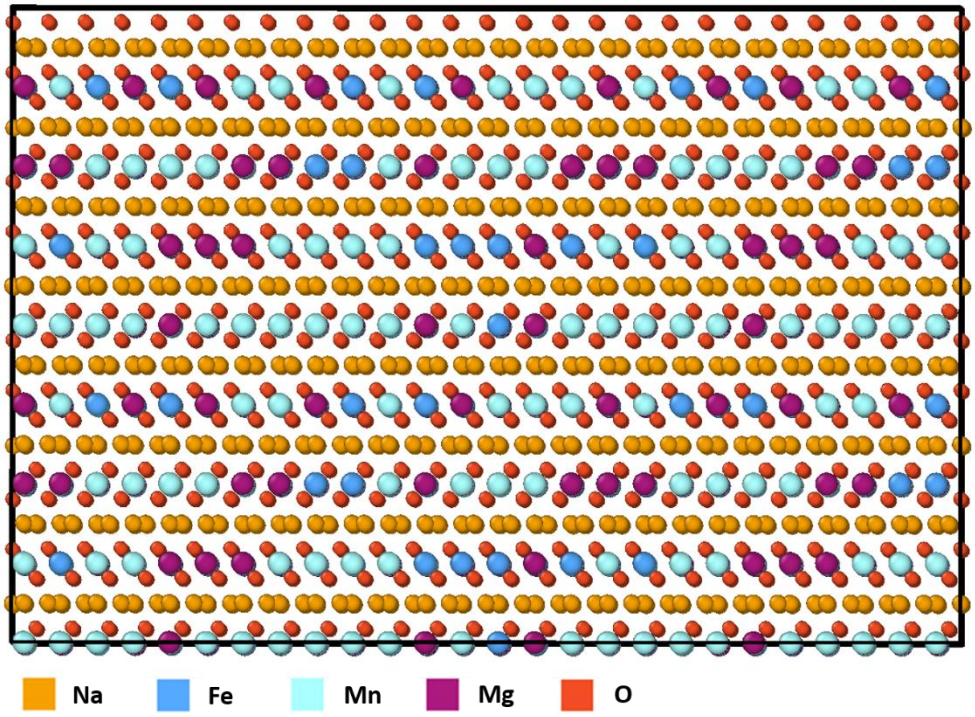

Supplementary Fig. 24 Side view of the initial structure model of NMMF used for MD simulations.

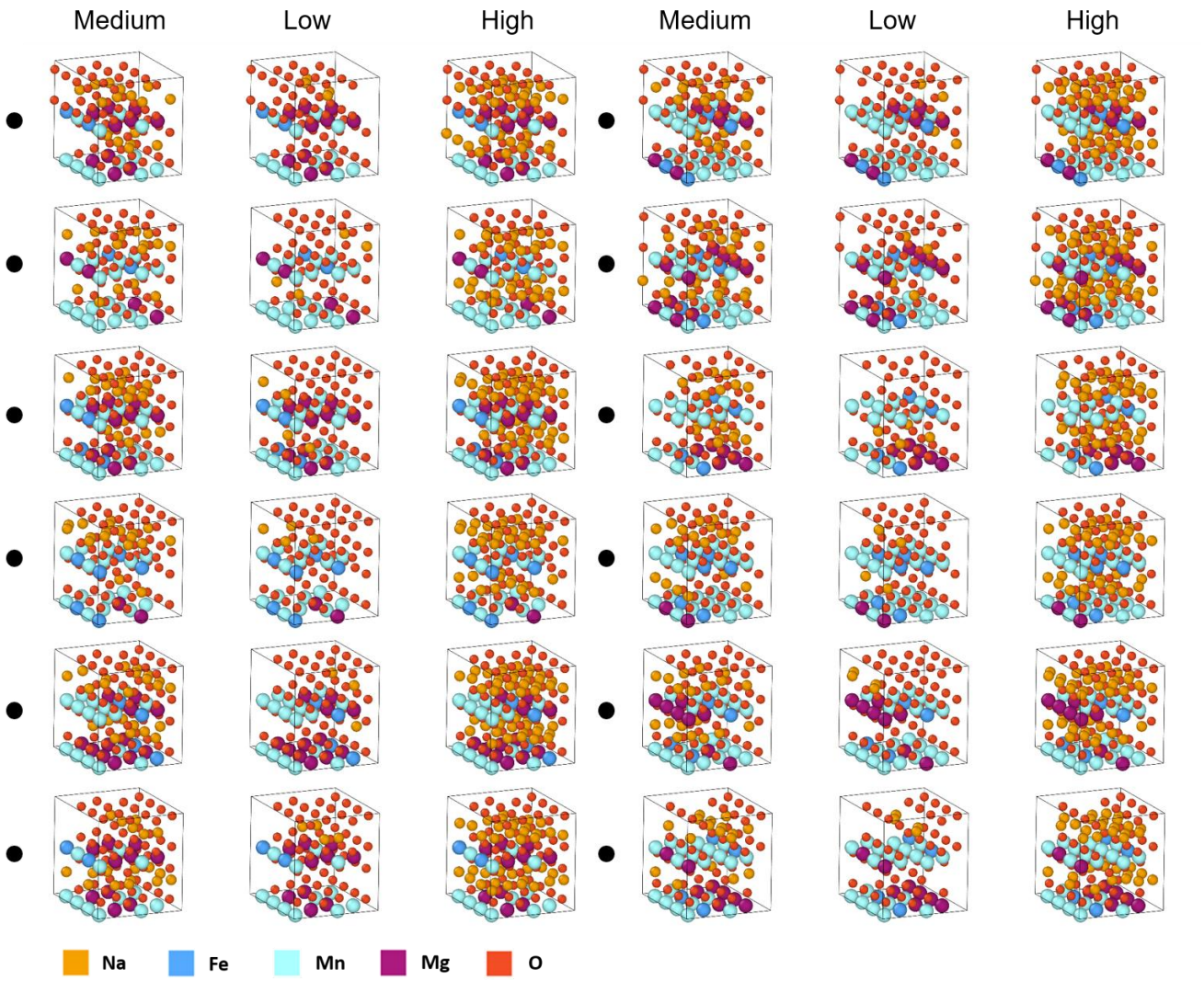

Supplementary Fig. 25 36 initial structures for AIMD simulations used to initialize the force field. Medium, low, high indicates the associated Na content of 50 %, 10 % and 100 %.

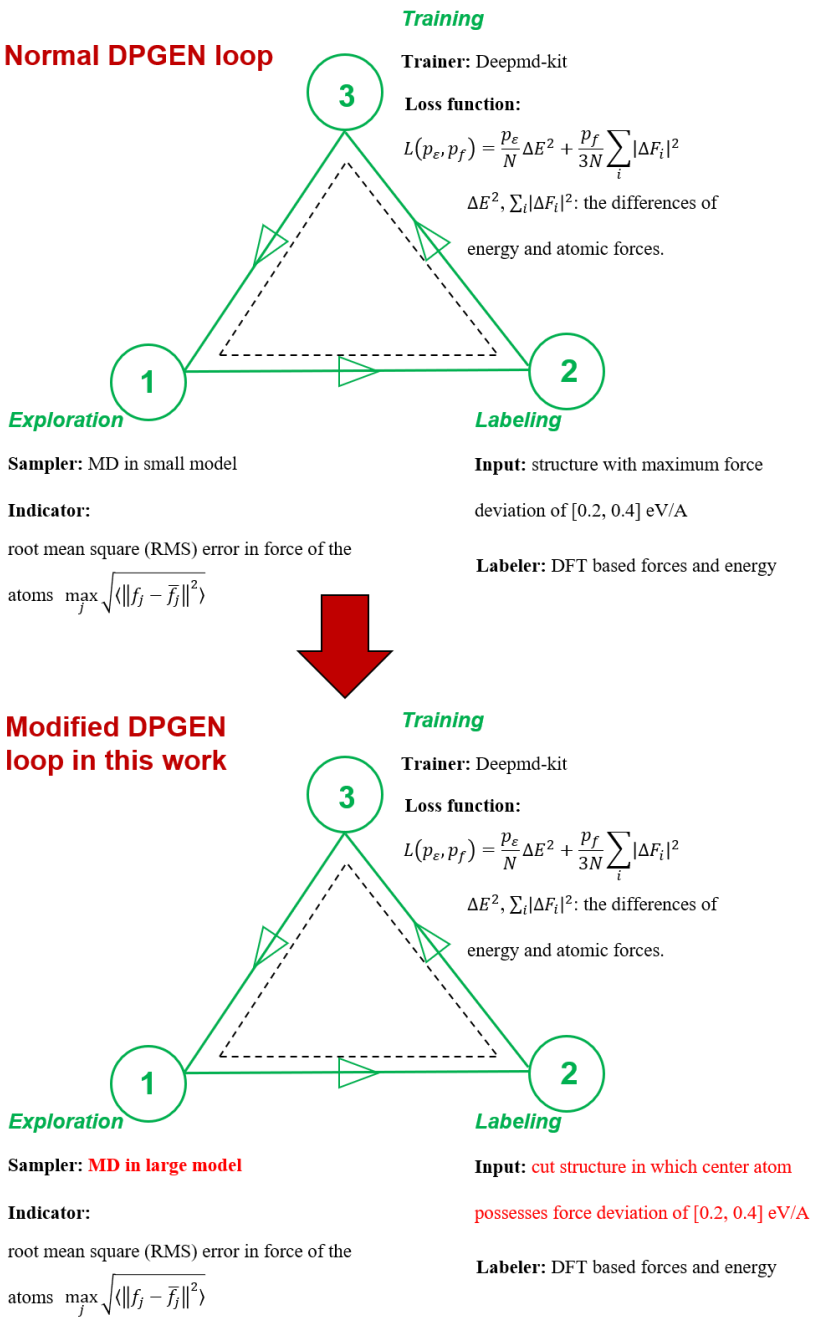

Supplementary Fig. 26 The scheme of the modified DPGEN in this work. The top and bottom panels indicate the normal and modified DPGEN loops, respectively.

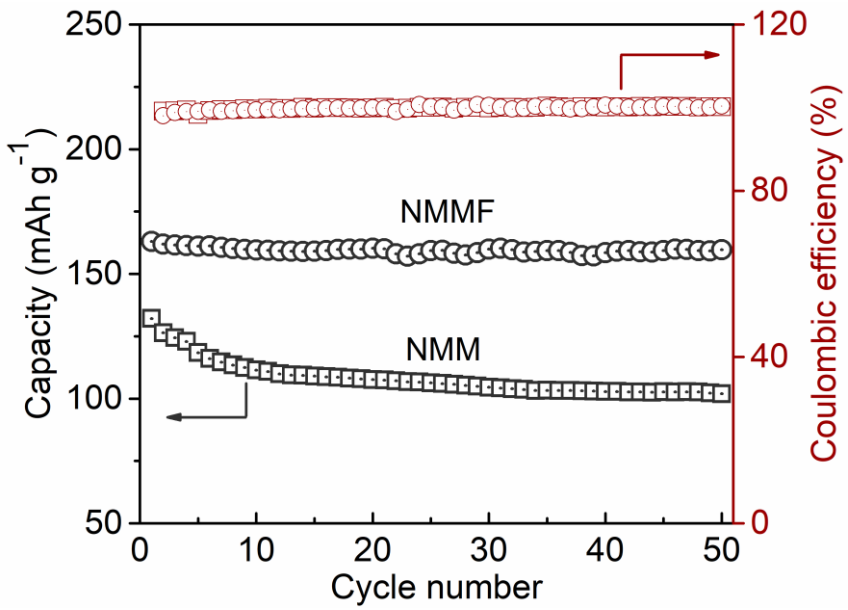

Supplementary Fig. 27 Comparison of the electrochemical stability of the NMM and NMMF electrodes. Voltage window: 1.5-4.5 V; current density: 200 mA g^{-1}.

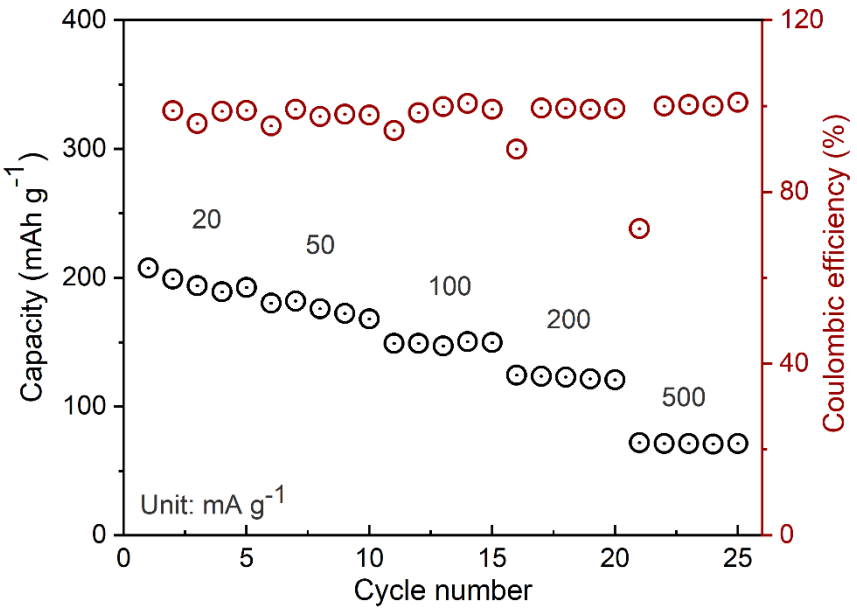

Supplementary Fig. 28 Rate performance of NMM electrode at the current densities of 20-500 mA g^{-1} in the voltage window of 1.5-4.5 V.

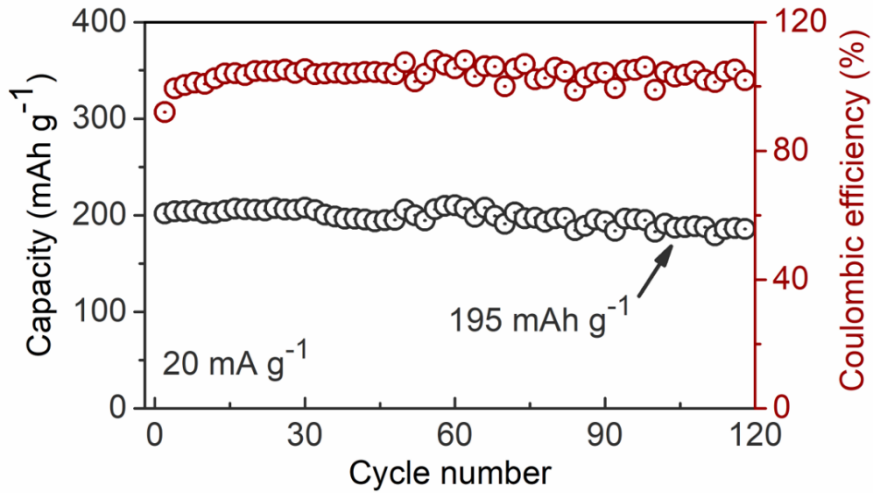

Supplementary Fig. 29 Electrochemical stability of NMMF half-cells at current densities of 20 mA g^{-1} in the potential window of 1.5-4.5 V.

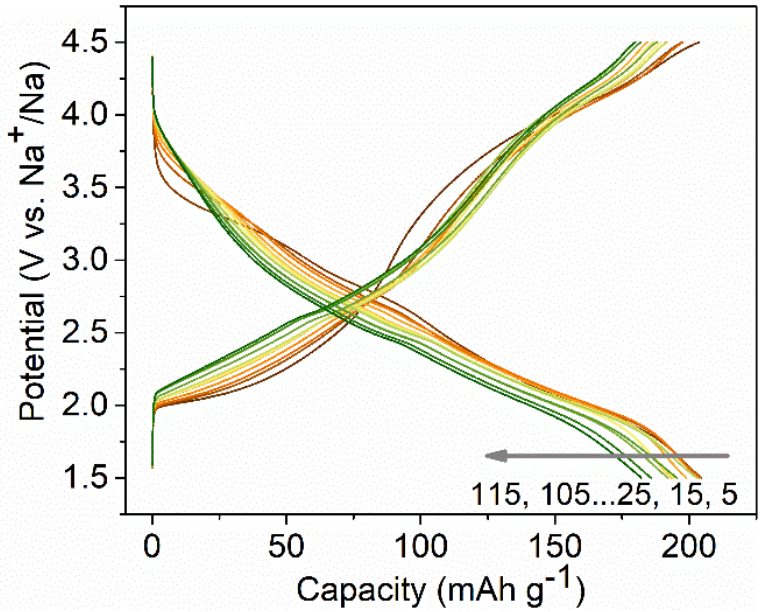

Supplementary Fig. 30 The charge-discharge profiles of NMMF electrode at 5th, 15th, 25th, 35th, 45th, 55th, 65th, 75th, 85th, 95th, 105th, and 115th cycles. Voltage window: 1.5-4.5 V; current density: 20 mA g^{-1}.

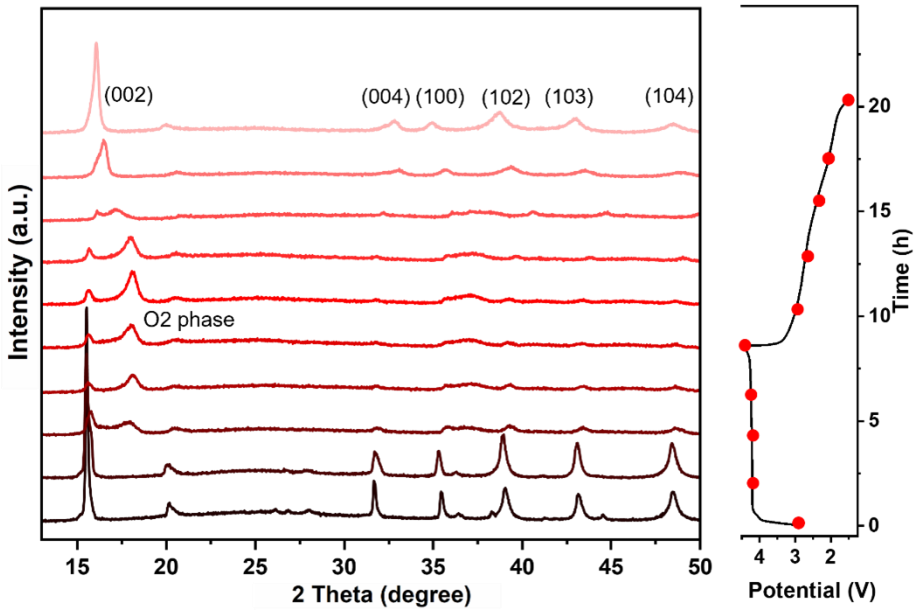

Supplementary Fig. 31 Ex-situ XRD patterns of NMM electrode and corresponding charge–discharge curves at 20 mA g^{-1} in the voltage window of 1.5-4.5 V. The ex-situ XRD patterns exhibit notable peak shifts and new reflections, indicating a significant phase transformation, consistent with a reversible P2–O2 type structural transition.

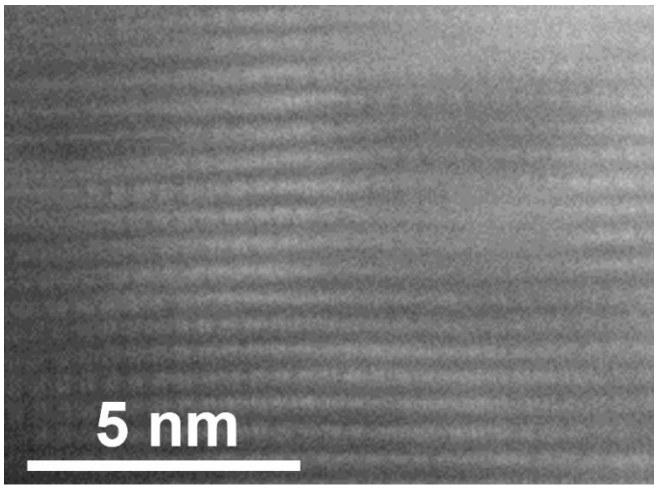

Supplementary Fig. 32 HAADF-STEM image of NMM after the first cycle.HAADF-STEM reveals that the honeycomb superstructure arising from the ordering of Li and Mn within the transition metal layer becomes partially disrupted after cycling, in agreement with the XRD.

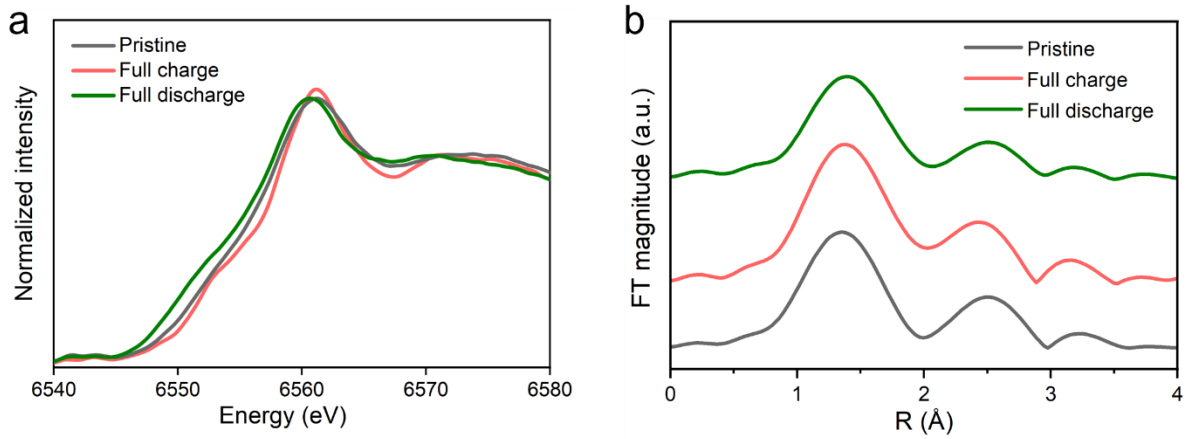

Supplementary Fig. 33 a, b, Ex-situ Mn K-edge XANES spectra (**a**) and the corresponding Fourier transformed EXAFS spectra (**b**) of NMM in the pristine, full charge, and full discharge states. During charging, the oxidation of Mn to a higher valence state does not lead to a shift in the Mn–O bond peak position. This behavior is attributed to a counterbalance between bond contraction induced by Mn oxidation and bond elongation resulting from the participation of lattice oxygen in the redox process. Upon discharge, Mn is reduced to an oxidation state lower than that of the pristine state, specifically from Mn^{4+} to Mn^{3+}, which typically elongates the Mn–O bond. Notably, while the lattice oxygen is restored to O^{2-} and Mn is further reduced toward Mn^{3+} in the discharged state, the Mn–O bond length exhibits only minimal change. This observation suggests the presence of $Mn^{3+}O^{6}$ Jahn–Teller distortions in the discharged structure.

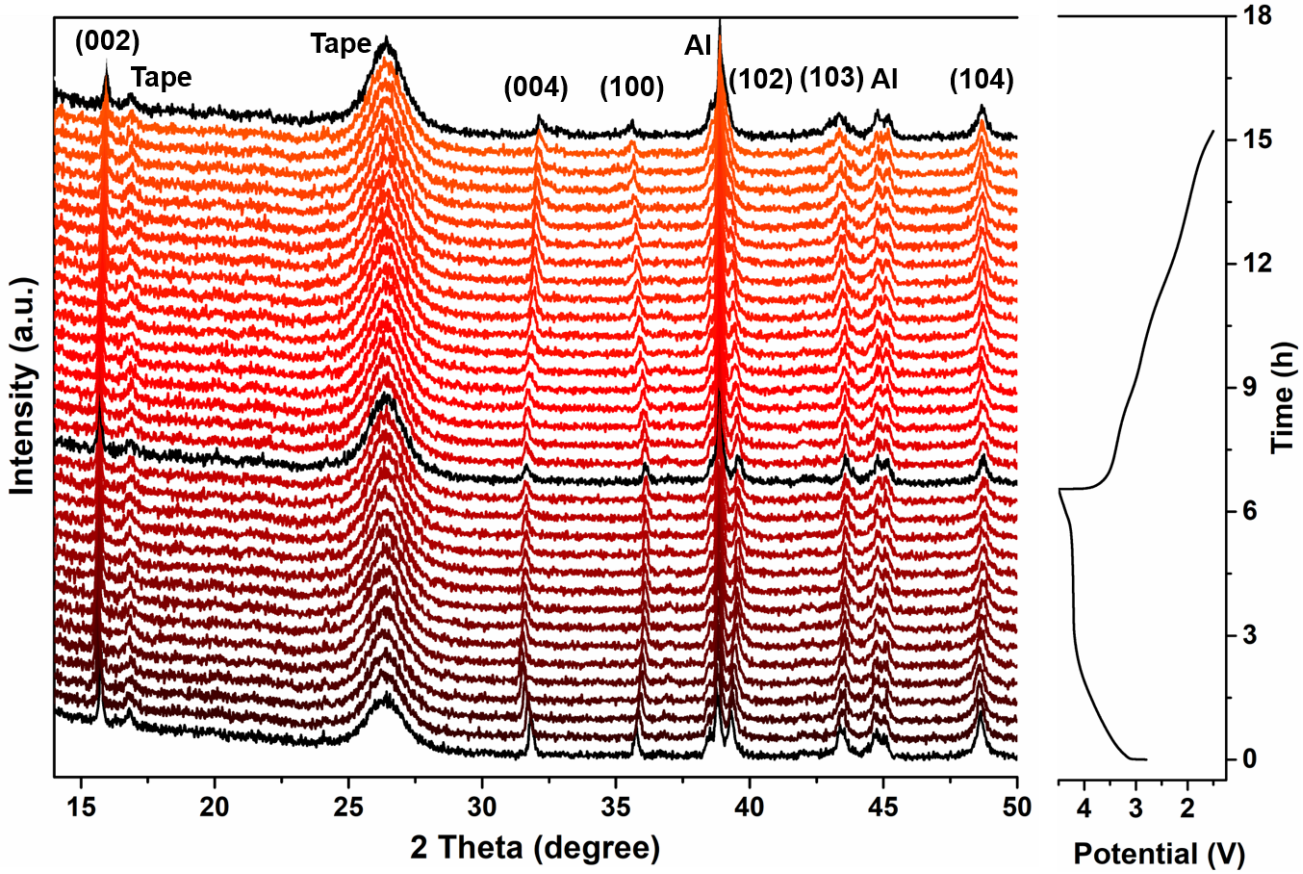

Supplementary Fig. 34 In-situ XRD patterns of NMMF electrode and corresponding charge–discharge curves at 20 mA g^{-1} in the voltage window of 1.5-4.5 V. In-situ XRD analysis shows minimal shifts in all main diffraction peaks, with no peak splitting or emergence of new diffraction peaks observed within 1.5-4.5 V, indicating a highly reversible solid-solution process.

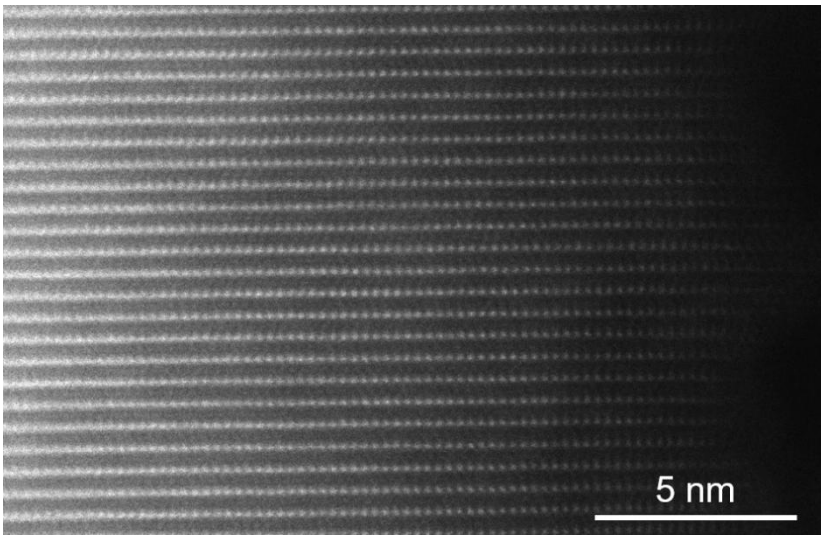

Supplementary Fig. 35 High-resolution HAADF-STEM image of NMMF after the first cycling process. The crystal structure is well maintained and no TM migration is found.

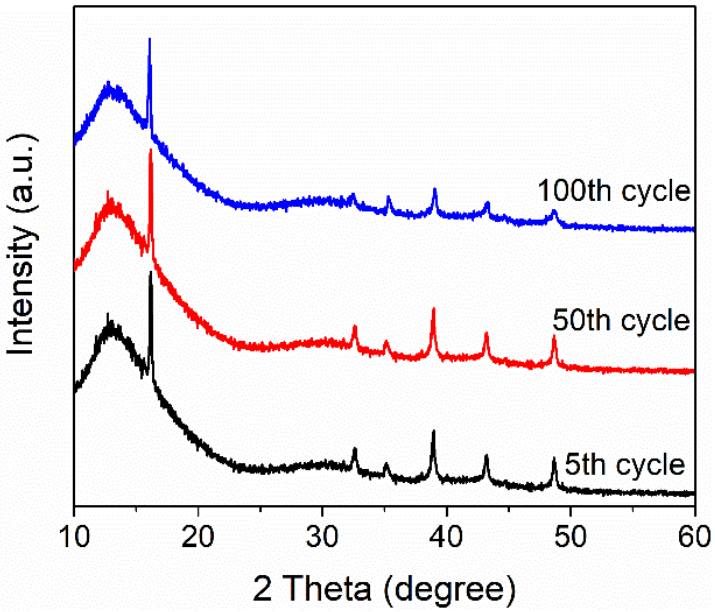

Supplementary Fig. 36 Ex-situ XRD patterns of NMMF electordes after 5, 50, and 100 cycles. Voltage window: 1.5-4.5 V; current density: 20 mA g^{-1}. The ex-situ XRD results show that NMMF maintains a stable crystal structure even after cycling.

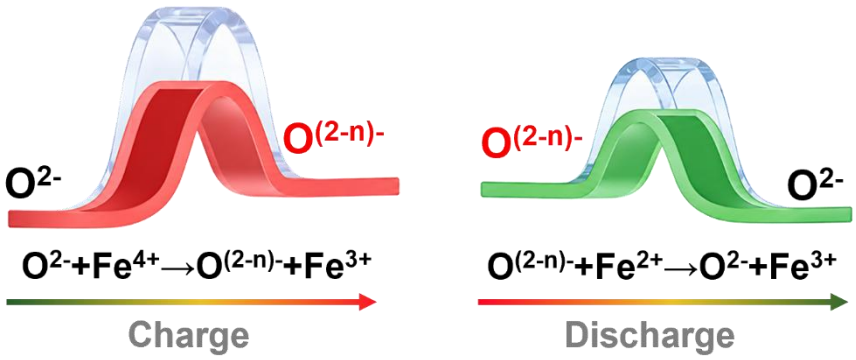

Supplementary Fig. 37 Schematic description of the mediated mechanism for the bifunctional RM in the NMMF during charge and discharge.

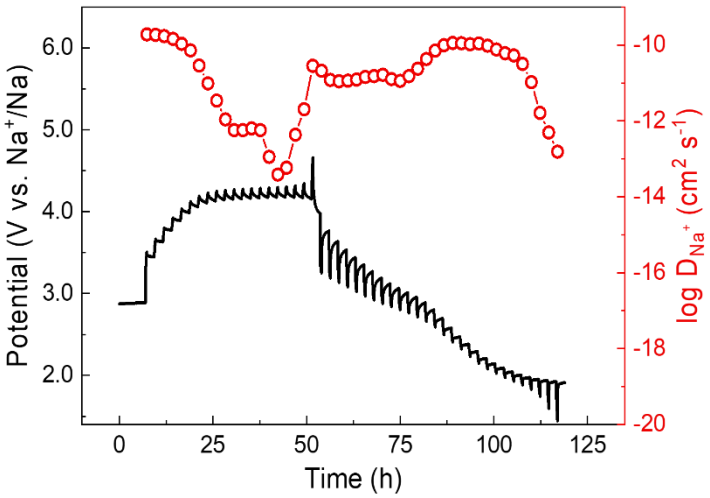

Supplementary Fig. 38 GITT curves and corresponding Na^+ diffusion coefficients of NMMF.

Supplementary Tables

Supplementary Table 1. Refined cell parameters of NMM and NMMF, based on Rietveld refinement of XRD.

Samples	NMM	NMMF
Space group	*P63/mcm*	*P63/mmc*
a (Å)	5.0415(4)	2.9079(7)
b (Å)	5.0415(4)	2.9079(7)
c (Å)	11.2232(4)	11.2116(5)
α (°)	90	90
β (°)	90	90
γ (°)	120	120
Volume ($Å^3$)	247.045	82.107
R_{wp} (%)	8.28	6.06
χ^2	3.79	4.58

Supplementary Table 2. Cell parameters of NMMF through refining NPD with the Rietveld refinement method.

Atom	Position	x	y	z	Uiso ($Å^2$)	Occupancy
Mg1	2a	0	0	0	0.03694	0.2500
Mn2	2a	0	0	0	0.03694	0.6191
Fe3	2a	0	0	0	0.03694	0.1309
Na4	2b	0	0	1/4	0.00843	0.1886
Na5	2d	2/3	1/3	1/4	0.05648	0.4633
O6	4f	1/3	2/3	0.09127	0.01721	1.0000
$a = b = 2.90845(18)$ Å, $c = 11.2073(6)$ Å, $V = 82.102(8)$ $Å^3$						
P63/mmc, $\alpha = \beta = 90°$, $\gamma = 120°$, $\chi^2 = 2.45$, Rp = 3.86%, Rwp = 5.50%						

Supplementary Table 3. Fitting parameters of room temperature ^{57}Fe Mössbauer spectra for NMMF electrodes under different charge/discharge states.

Samples	Sub-spectra	IS (mm s^{-1})	QS (mm s^{-1})	Linewidth (mm s^{-1})	Area (%)	Species
pristine	1	0.337(1)	0.706(3)	0.154(2)	100.0	$Fe^{3+}O_6$
Ch-4.25V	1	0.328(14)	0.763(23)	0.194(22)	86.8	$Fe^{3+}O_6$
	2	-0.196(70)	0.661(12)	0.161(11)	13.2	$Fe^{4+}O_6$
Ch-4.5V	1	0.329(13)	0.746(25)	0.213(21)	92.2	$Fe^{3+}O_6$
	2	-0.196(23)	0.793(30)	0.208(34)	7.8	$Fe^{4+}O_6$
Dis-2.75V	1	0.345(62)	0.749(12)	0.188(90)	93.3	$Fe^{3+}O_6$
	2	0.537(75)	1.731(16)	0.171(12)	6.7	$Fe^{2+}O_6$
Dis-1.5V	1	0.337(2)	0.728(3)	0.162(2)	100.0	$Fe^{3+}O_6$

Supplementary Table 4. Fitting parameters of 77 K ^{57}Fe Mössbauer spectra for charged NMMF electrode.

Samples	Sub-spectra	IS (mm s^{-1})	QS (mm s^{-1})	Linewidth (mm s^{-1})	Area (%)	Species
Ch-4.25V	1	0.35(1)	1.01(3)	0.35(9)	13.3	$Fe^{3+}O_6$
	2	-0.23(1)	1.13(2)	0.50(7)	13.9	$Fe^{4+}O_6$
	3	0.38(9)	-0.13(1)	0.80(9)	72.9	$Fe^{3+}O_6$

Supplementary Table 5. The energy density comparison between the NMMF ‖ HC pouch cell and other sodium-based cathode ‖ HC pouch cells reported in previous literatures.

Full cell (cathode‖anode)	Cell capacity (Ah)	Energy density (Wh kg^{-1})	Reference
NFVPP‖HC	1.97	90	S12
NFPP‖HC	13	91.7	S13
NMNCO‖HC	1	91.9	S14
NVPF‖HC	0.85	106	S15
NVMP‖HC	8.61	112.75	S16
NNFMO‖HC	0.9	117	S17
NFMO‖HC	2.94	120	S18
NVP‖HC	5	129	S19
NLNMO‖HC	2	130	S20
NNFMO‖HC	3	132.2	S21
NVP‖HC	0.1	135.2	S22
NFMO‖HC	1.1	137	S23
NNFMO‖HC	5.02	145	S24
HENMO‖HC	3.5	155.1	S25
NLFMO‖HC	1.3	165	S26
NFMO‖HC	5.53	170	S18
NMMFO‖HC	15.8	206	This work

Supplementary References

S1. Li, B. et al. Correlating ligand-to-metal charge transfer with voltage hysteresis in a Li-rich rock-salt compound exhibiting anionic redox. *Nat. Chem.* **13**, 1070-1080 (2021).

S2. Li, B. et al. Capturing dynamic ligand-to-metal charge transfer with a long-lived cationic intermediate for anionic redox. *Nat. Mater.* **21**, 1165-1174 (2022).

S3. Cheng, C. et al. Enhancing the reversibility of lattice oxygen redox through modulated transition metal-oxygen covalency for layered battery electrodes. *Adv. Mater.* **34**, 2201152 (2022).

S4. Yu, Y. et al. Revealing the anionic redox chemistry in O3-type layered oxide cathode for sodium-ion batteries. *Energy Storage Mater.* **38**, 130-140 (2021).

S5. Paidi, A. K. et al. Unravelling the nature of the intrinsic complex structure of binary-phase Na-layered oxides. *Adv. Mater.* **34**, 2202137 (2022).

S6. Zhang, K. et al. Manganese based layered oxides with modulated electronic and thermodynamic properties for sodium ion batteries. *Nat. Commun.* **10**, 5203 (2019).

S7. Zhan, C. et al. Enabling the high capacity of lithium-rich antifluorite lithium iron oxide by simultaneous anionic and cationic redox. *Nat. Energy* **2**, 963-971 (2017).

S8. McCalla, E. et al. Understanding the roles of anionic redox and oxygen release during electrochemical cycling of lithium-rich layered Li_4FeSbO_6. *J. Am. Chem. Soc.* **137**, 4804-4814 (2015).

S9. Sun, D. et al. A solution-phase bifunctional catalyst for Lithium-oxygen batteries. *J. Am. Chem. Soc.* **136**, 8941-8946 (2014).

S10. Park, J. B. et al. Redox mediators for Li–O_2 batteries: status and perspectives. *Adv. Mater.* **30**, 1704162 (2018).

S11. Yabuuchi, N. et al. P2-type $Na_x[Fe_{1/2}Mn_{1/2}]O_2$ made from earth-abundant elements for rechargeable Na batteries. *Nat. Mater.* **11**, 512-517 (2012).

S12. Zhang, H. et al. Structurally Modulated $Na_{4-x}Fe_{3-x}V_x(PO_4)_2P_2O_7$ by Vanadium Doping for Long-Life Sodium-Ion Batteries. *ACS Sustainable Chem. Eng.* **12**, 5310-5318 (2024).

S13. Lu, T. et al. Shape Engineering: Morphological Size Optimization for High-Pressure Solid Density $Na_3Fe_2(PO_4)P_2O_7$ Cathode Material Preparation and Performance Investigation. *ACS Appl. Energy Mater.* **7**, 6986-6995 (2024).

S14. Li, M. et al. Tailoring Cu-rich surface spinel phase for high-performance O3-type layered cathode materials for sodium-ion batteries. *Nano Energy* **123**, 109375 (2024).

S15. Lakienko, G. P. et al. Design of the Particle Size and Morphology of Hard Carbon Anode Materials for Sodium-Ion Batteries Through Hydrothermal Carbonization. *J. Electrochem. Soc.* **171**, 060512 (2024).

S16. Tang, X. et al. A novel kilogram-scale preparation method of the $Na_{3.5}V_{1.5}Mn_{0.5}(PO_4)_3$ cathode material with excellent performance for sodium-ion pouch cells. *J. Mater. Chem. A* **12**, 22286-22298 (2024).

S17. Li, Y. et al. Sole-Solvent High-Entropy Electrolyte Realizes Wide-Temperature and High-Voltage Practical Anode-Free Sodium Pouch Cells. *Adv. Mater.* **37**, 2419764 (2025).

S18. Tang, Y. et al. Sustainable layered cathode with suppressed phase transition for long-life sodium-ion batteries. *Nat. Sustain.* **7**, 348-359 (2024).

S19. Hou, X. et al. Weak coulomb interaction between anions and Na^+ during solvation enabling desirable solid electrolyte interphase and superior kinetics for HC-based sodium ion batteries. *Chem. Eng. J*. **453**, 139932 (2023).
S20. Zhang, T. et al. Converting Residual Alkali into Sodium Compensation Additive for High-Energy Na-Ion Batteries. *ACS Energy Lett.* **8**, 4753-4761 (2023).
S21. Liu, G. et al. Practical and Versatile Sodium-Ion Batteries Realized With Nitrile-Based Electrolytes. *Adv. Energy Mater.* **15**, 2405319 (2025).
S22. Bhawana, K. et al. Endorsing Na^+ storage mechanism in low tortuosity, high plateau capacity hard carbon towards development of high-performance sodium-ion pouch cells. *Carbon* **214**, 118319 (2023).
S23. Wang, X. et al. Anion-mediated approach to overcome oxidation in ether electrolytes for high-voltage sodium-ion batteries. *Nat. Commun.* **16**, 2536 (2025).
S24. Liao, Y. et al. Pentafluoro(phenoxy)cyclotriphosphazene Stabilizes Electrode/Electrolyte Interfaces for Sodium-Ion Pouch Cells of 145 Wh Kg^{-1}. *Adv. Mater.* **36**, 2312287 (2024).
S25. Gao, S. et al. Reversible Phase Transition of an Oxide Cathode in High-Voltage Sodium-Ion Batteries. *ACS Energy Lett.* **10,** 4140-4147 (2025).
S26. Wang, X. et al. Achieving a high-performance sodium-ion pouch cell by regulating intergrowth structures in a layered oxide cathode with anionic redox. *Nat. Energy* 9, 184-196 (2024).